PHYSICAL REVIEW A **102**, 033110 (2020)

Optimization of crystal high-order harmonic generation by tailoring the nonuniform irradiations

Ling-Jie Lü[1,2] and Xue-Bin Bian[1,*]
[1]State Key Laboratory of Magnetic Resonance and Atomic and Molecular Physics, Wuhan Institute of Physics and Mathematics, Innovation Academy for Precision Measurement Science and Technology, Chinese Academy of Sciences, Wuhan 430071, China
[2]School of Physical Sciences, University of Chinese Academy of Sciences, Beijing 100049, China

(Received 16 June 2020; accepted 31 August 2020; published 18 September 2020)

High-order harmonic generation (HHG) is expected to produce high-quality coherent ultrashort light sources. We propose a scheme similar to laser mode locking to selectively enhance and compress HHG in crystals through nonuniform illuminations and phase matching. The selective enhancement of harmonics reflects attosecond-resolved electron dynamics. And these harmonic characteristics originate from the interference of harmonics from different lattices. It paves the way for the practical application of solid HHG with high conversion efficiencies and the detection of electron-hole dynamics with ultrahigh spatial-temporal resolution.

DOI: 10.1103/PhysRevA.102.033110

I. INTRODUCTION

The laser, first invented by Maiman in 1960, has changed the world greatly. Mode-locking technology plays a key role to achieve ultrashort laser pulses [1]. The indirect laser, high-order harmonic generation (HHG) induced by intense femtosecond lasers in the gas and condensed phases, has been widely studied [2–13]. To achieve the high yield of HHG, phase matching of different atoms or molecules at different sites should be considered [14–23]. However, low efficiency is still the bottleneck of attosecond lasers based on gas samples. Crystals with periodicity, high density, and inherent directionality are expected to produce efficient HHG sources [7,8,20,24]. The interband mechanism of crystal HHG is similar to that in gases: it has the unique chirped structures (quantum trajectories) corresponding to the recombination of electrons and holes [25]. Although some characteristics of crystal HHG, such as different dependence of the cutoff energy on the driving laser parameters [26,27] and the double-plateau structure [28], have been demonstrated, the expected high conversion efficiency still has large room to improve. As a broad-bandwidth source, HHG may be interesting in a specific narrow spectral range in some applications. Selective enhancement of HHG is appealing.

The inherent harmonic phases related to the driving light intensities play a key role in the formation of clear harmonic spectra and the control of quantum trajectories [15,21,23]. However, for the detection of dynamics with ultrahigh spatial-temporal resolution and the realization of high conversion efficiency in crystal HHG, the significance of nonuniform irradiation has not been well revealed. In this work, we find that, although the harmonics induced by a uniform field are not in phase [15], the interband harmonic fields induced by nonuniform irradiations [29–31] are similar to the longitudinal modes in lasers and their phases could be locked. The mechanism similar to laser mode locking results in the selection of HHG in the time and frequency domains. When additional phases are not considered, the ultraviolet pulses are far from the in-phase position (IPP), which significantly inhibits the yield of crystal HHG. However, the addition of appropriate optical path differences (OPD) in the range of ≈100 nm could shift the IPP in the range of ≈1000 nm, thus selectively enhancing and compressing the ultraviolet pulses. This demonstrates the feasibility of observing and controlling HHG within the time resolution of attoseconds. We notice that the nonlocality limits the electron diffusion in crystals, so intense radiation is expected in the long trajectories of crystal HHG when an appropriate OPD is compensated. Thus, the inherent advantages of crystal HHG can be utilized. Moreover, we find that parts of a Bloch electron can evolve independently under the drive of ultrafast inhomogeneous field, and the harmonic characteristics caused by the nonuniform irradiation actually originates from the interference in real space. This is of great significance in the study of nanometer-resolution electron dynamics in solids.

The calculation details are shown in Sec. II. In Sec. III, we demonstrate the nonuniform field-induced HHG and illustrate the mode-locking mechanism in HHG. Our work is summarized in Sec. IV.

II. METHODS FOR SOLVING TIME-DEPENDENT SCHRÖDINGER EQUATION

A. Velocity gauge

The one-dimensional Bloch states in a lattice $[-a_0/2, a_0/2]$ are obtained by calculating the stationary Schrödinger equation using Bloch theorem, and the time-dependent Schrödinger equation (TDSE) is solved by the Crank-Nicolson method under the velocity gauge [32]. We choose 250 Bloch states within the first Brillouin zone (BZ) on the highest valence band as the initial states and integrate harmonics throughout the BZ. Atomic units are used unless stated otherwise.

---

[*] xuebin.bian@wipm.ac.cn

The driving field used in this paper is

$$\tilde{F}(F,t) = Fe^{-4\ln(2)\frac{t^2}{\tau^2}}\sin(\omega t+\varphi), \tag{1}$$

where τ is the full width at half maximum (FWHM), and $\varphi = 0$ is the carrier-envelope phase (CEP). Once the time-dependent wave function Ψ is obtained, the harmonic field can be calculated by the dipole acceleration

$$\tilde{a}(F,t) = \int_{BZ} dk \int_{RS} dx \Psi^* \frac{\partial V}{\partial x}\Psi, \tag{2}$$

where V is the periodic potential. The Mathieu-type potential is used in this work. The inner integral range is the whole real space, and the outer integral range is the whole BZ.

B. Length gauge

The Bloch states are obtained by the same method, but real space here extends over $[-500a_0, 500a_0]$, and the TDSE is calculated in the length gauge by using the split-operator method. The peak value of the driving field in real space is a Gaussian distribution. The inhomogeneous driving field can be written as

$$\hat{F}(x,t) = F_0 e^{-4\ln(2)\left(\frac{x^2}{\sigma^2}+\frac{t^2}{\tau^2}\right)}\sin(\omega t+\varphi), \tag{3}$$

where σ is the FWHM of the field in real space, which reflects the inhomogeneity of the driving field. If F in Eq. (1) represents the spatial-dependent field peak strength of this inhomogeneous field, then

$$F = F_0 e^{-4\ln(2)\frac{x^2}{\sigma^2}}. \tag{4}$$

Two hundred and fifty Bloch states in the BZ are uniformly sampled as the initial states, and harmonics are integrated throughout the BZ. To weaken the reflection of wave packets at the boundary, the wave function is multiplied by an absorption function of the form $\cos^{1/8}$ with $|x| > 495a_0$ at each time step. To further avoid the influence of the edge, a part of the wave function near the boundaries is ignored when calculating the harmonics.

To extract the spatial information of harmonics, we add a Gaussian filtering $G(x_0)$ in real space with the FWHM of $5a_0$, where x_0 is the center of the filtering. The selection of the filtering width is based on the consideration of smoothing out the oscillations in lattices while preserving the oscillations on the nanometer scale. We get the real-space-dependent dipole acceleration

$$\hat{a}(x_0,t) = \int_{BZ} dk \int_{RS} dx \Psi^* \frac{\partial V}{\partial x}\Psi G(x_0), \tag{5}$$

which depicts the harmonic space profile.

III. RESULT AND DISCUSSION

To illustrate the uniform-field-induced HHG, we solve the TDSE under the velocity gauge first, as described in Sec. II A. The HHG spectrum calculated by using the driving field with a wavelength of 3250 nm, the field peak strength $F = 0.003$ a.u., and the FWHM of five cycles is shown in Fig. 1(b) by a black curve. Similar to the calculations in many papers [8,9], there are no clear integer peaks in the first plateau.

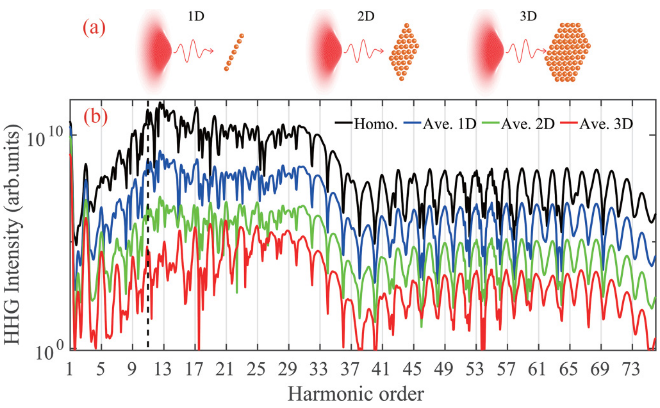

FIG. 1. (a) Schematic diagrams of nonuniform illumination of the driving field. The driving pulses with Gaussian field strength in the cross section irradiate the 1D, 2D, and 3D materials, respectively. (b) HHG spectra induced by the uniform driving fields (black), averaged with 1D (blue), 2D (green), and 3D (red) weights, respectively. The vertical dashed line indicates the minimum band gap.

Imitating the situation in atomic HHG, the driving field is considered to be uniform in a small range. We use the weighted average of harmonics induced by the uniform driving fields to represent the harmonics induced by a nonuniform field, the weight $W(F)$ is the atomic population as a function of the driving field intensity. So the weighted average harmonic spectrum is $I(\omega) = |FT[\int_0^{F_0} dF W(F)\tilde{a}(F,t)]|^2$, where FT represents Fourier transform. 180 F values are uniformly sampled from 0 to $F_0 = 0.003$ a.u. We assume several atomic populations irradiated by an inhomogeneous field to investigate the nonuniform-irradiation effects. The one-, two-, and three-dimensional (1D, 2D, and 3D) weights shown in Fig. 2(a) are explained in Appendix A, which respectively represent the atomic populations in the 1D, 2D, and 3D materials (considering the laser attenuation in the propagation) irradiated by a laser with Gaussian intensity distribution in the cross section, as exhibited in Fig. 1(a). The weighted average harmonic spectra are shown in Fig. 1(b). With increasing dimensions, the harmonic intensity in the plateaus is obviously weakened and the integer harmonic peaks become clear in the first plateau.

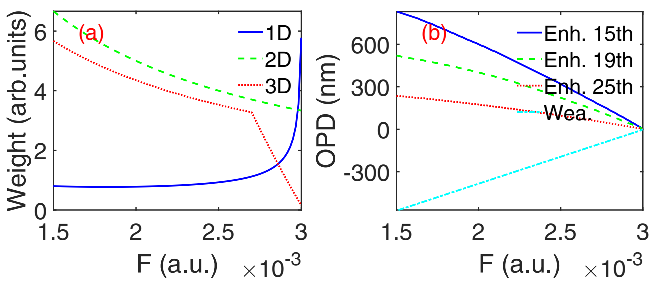

FIG. 2. (a) The 1D (blue solid line), 2D (green dashed line), and 3D (red dotted line) weights. (b) The optimized OPD for enhancing the 15th (blue solid line), 19th (green dashed line), and 25th (red dotted line) harmonics, respectively. The cyan dot-dashed line represents the OPD for weakening harmonics.

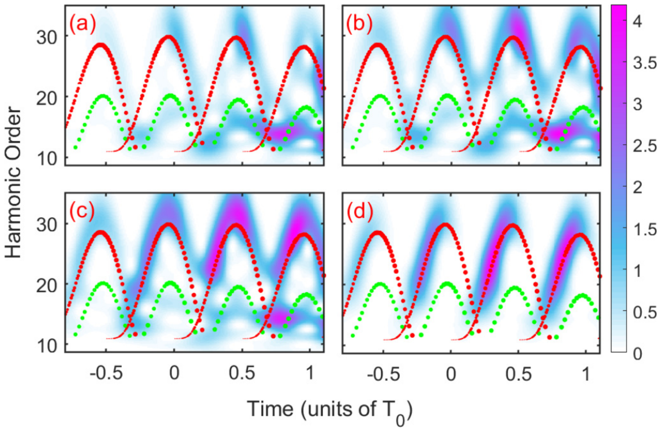

FIG. 3. (a) Time-frequency analysis of the uniform-field induced harmonics and averaged harmonics with (b) 1D, (c) 2D, and (d) 3D weights. The color scale is logarithmic. The red and green dots indicate the semiclassical trajectories of the first and second recombinations with $F = 0.003$ a.u. The size of the dots is proportional to the driving field strength at the tunneling time.

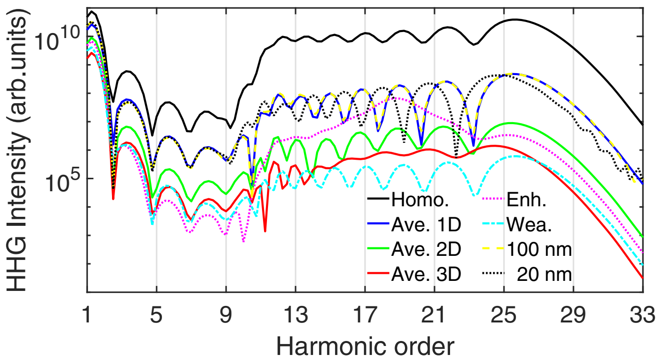

FIG. 4. Harmonic spectra in one-cycle lasers. The solid curves are the same as those in Fig. 1, but the FWHM of the driving field is one cycle, CEP = 0 rad. The magenta dotted and cyan dot-dashed curves represent the enhanced and weakened spectra using the 2D weight, respectively. The yellow dashed and black dotted curves represent spectra obtained under the length gauge, the FWHM of the driving field in real space are 100 and 20 nm, respectively.

Figure 3 shows the time-frequency analysis [33] of the harmonics in Fig. 1. These inherent chirp structures are consistent with the semiclassical trajectories obtained by the saddle-point approximation (marked by dots) [25]. Analogous to atomic HHG, the front and back of the energy maxima in the first recombination are called the short and long trajectories, respectively. In Fig. 3(a), the radiation in long trajectories is much brighter than that in short trajectories, and the trajectories of the second recombination are also obvious. This is because most electrons tunnel near the peak of driving fields [34] and they recombine near the end of the long trajectory, according to the semiclassical model [25]. When the effect of a nonuniform driving field is not considered, as far as we know, the mechanisms leading to the attenuation of long trajectories are from the electron diffusion [15,35] and dephasing [8]. Diffusion of tunneling electrons in 3D space results in obvious attenuation of long trajectories and multiple recombination trajectories for atomic HHG. However, the diffusion of nonlocal electrons (Bloch electrons distributed in infinite space in our calculations) is negligible, and the electrons in the actual crystals are obviously nonlocal. Some works [23,36] indicate that the electrons driven by intense fields in crystals can maintain coherence within one optical cycle. Therefore, when T_0 is comparable to or shorter than the dephasing time, intense radiation is expected to be obtained in long trajectories for crystal HHG. This is the manifestation of electron nonlocality, which distinguishes crystal HHG from atomic HHG.

Frequency doubling peaks in the frequency domain are the responses of the periodicity in the time domain. The intense radiation in the long and multiple recombination trajectories increases the aperiodicity of harmonics. This is the reason why the simulated crystal HHG spectra (such as Ref. [8]) lack clear integer peaks when using the driving pulse with a Gaussian envelope. Note that, if the driving pulse with a trapezoidal envelope is adopted (such as Ref. [37]), the harmonic spectrum naturally has a clear integer multiple peak, because the electric field itself has strict periodicity. However, as shown in Figs. 3(b)–3(d), the radiation in the long and multiple recombination trajectories is effectively suppressed after the average. This results in a significant reduction in the harmonic yield above the band gap and clear harmonics.

To reveal the dynamics with short time resolution, we use a single-cycle (FWHM) pulse in the TDSE. The solid black curve in Fig. 4 indicates the HHG spectrum induced by the uniform driving field with CEP = 0 rad, its time-frequency analysis is presented in Fig. 5(a). The pulse is so short that we can clearly see a continuous chirp structure composed of a bright long trajectory and a dim short trajectory, and multiple recombinations disappear. In the spectrum, there is a weak structure of interference between the long and short trajectories in the first plateau and the odd peaks caused by the interference between intercycles disappear. However, the interference structure is more obvious in the average harmonic

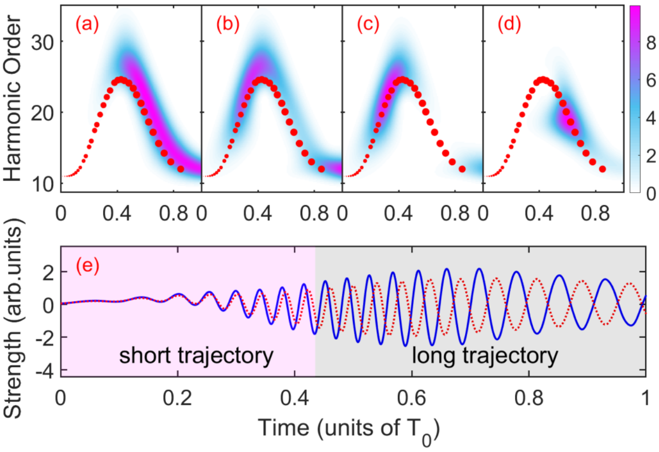

FIG. 5. Time-frequency analysis of the harmonics shown in Fig. 4. (a) The uniform-field-induced harmonics. (b)–(d) Averaged harmonics with 2D weight, 3D weight, and 2D weight with a compensation OPD. The color scale is logarithmic. (e) The harmonic temporal profile $\tilde{a}(F, t)$ with $F = F_0 = 0.0030$ (blue solid line) and 0.0028 a.u. (red dotted line). The pink and gray shadows mark the range of short and long trajectories, respectively.

spectra with 1D and 2D weights (shown in Fig. 4 with solid blue and green lines, respectively), because the nonuniform irradiation weakens the long trajectory [as shown in Fig. 5(b)]. When 3D weight is used, the interference structure (shown in Fig. 4 with a solid red line) is weakened again due to the very dim long trajectory [as shown in Fig. 5(c)]. Thus, the interference between the long and short trajectories is sensitive to the nonuniformity of the driving field, which can be controlled by adjusting the distribution of the driving-field intensity.

To see the selection mechanism of the quantum trajectories, the harmonic temporal profiles induced by driving fields with $F = 0.0030$ and 0.0028 a.u. are shown in Fig. 5(e). Since the signals in multiple recombination and higher plateaus are negligible, the oscillations in the figure are the short and long trajectories contributing to the first plateau. The inherent harmonic phase comes from the phase differences between the recombined electrons and holes [4,8]. These phase differences are zero at the starting point of the short trajectory (generally at the time when the driving field crosses zero, here means $t = 0$), since the tunneling and recombination occur simultaneously. This means that all the harmonic fields induced by the driving fields with different intensities have the same phase at these times (called IPP in the paper, here is $t = 0$). Since the phase differences between electrons and holes accumulate during their separation and depend on the driving-field strength, the two harmonic temporal profiles gradually diverge afterwards (the attenuation of the driving light leads to the phase delay and intensity attenuation of harmonics), as shown in Fig. 5(e). Long trajectories far from IPP are greatly suppressed due to frequent destructive interferences after averaging the harmonics. Although the harmonics near IPP (mainly short trajectories) remain, the intensity itself is weak. This is reminiscent of the laser mode-locking mechanism. Interestingly, the harmonic fields induced by the driving fields with different intensities are similar to longitudinal modes in lasers, but these "modes" have chirps. Furthermore, the nonuniform weight can adjust this mechanism, which leads to harmonic conversion efficiency decreasing with the increase of dimensions. For example, the laser attenuation in the propagation causes a steep drop in 3D weight, which effectively compensates for the attenuation of the harmonic intensity, thus greatly suppressing the harmonic radiations [23,31].

In addition to the inherent phase, the laser propagation in vacuum (an example is discussed in Appendix B) and the refractive index of the medium generally introduce additional phases, which can compensate for the phase delay caused by the attenuation of the driving fields. We assume that the optical path from the position where the harmonics are generated (the position of the molecules or lattices that radiate the harmonics) to infinity (the position of the detector, because its distance from the material is far enough relative to the spot size irradiated on the material) is $P(F)$, which is a function of the field peak strength of the driving laser because of the spatial dependence of the laser intensity. Then, the OPD is defined as

$$D = P(F_0) - P(F). \tag{6}$$

One can see in Fig. 5(e) that, if the harmonic induced by the weaker driving field is shifted a little to the left to compensate for the lagging phases [it means adding an $D(F = 0.0028) > 0$, which causes the harmonic represented by the red dotted line to reach the detector earlier; that is, to shift to the left on the time axis], the IPP will move to the right, towards the long trajectory. As an example, a proper OPD is added to each harmonic in the averaged harmonic with 2D weight, which ensures that the 19th harmonic is fully enhanced, so that the spectrum with the enhanced 19th harmonic (the magenta dot curve in Fig. 4) is obtained. The time-frequency analysis of the enhanced harmonic is shown in Fig. 5(d). The harmonic is enhanced by more than an order of magnitude, meanwhile it is compressed by nearly an order of magnitude in the time domain. Figure 2(b) shows the optimized OPD for enhancing the 15th, 19th, and 25th harmonics. One can see that the optimized OPD approximates straight lines with specific slopes. The gradual-to-steep process of these lines causes IPP to move from the beginning of the short trajectory to the end of the long trajectory. Since the enhanced pulses come from the bright long trajectory with a negative chirp, their central frequencies decrease with the increase of OPD. When a negative OPD [the cyan dot-dashed curve in Fig. 2(b)] is used, the yield can be greatly attenuated (the cyan dot-dashed curve in Fig. 4), because the IPP moves to the left, away from the trajectories. This shows that the mode-locking mechanism can selectively enhance and compress harmonics and provides a way to modulate the ultraviolet coherent light in the frequency domain. The enhancement of harmonics in the frequency domain comes from the selection in the subcycle time domain, thus realizing the detection of attosecond resolution dynamics. Besides, the disappearance of quantum trajectories in Fig. 5(d) implies that the chirp of interband harmonics can be reduced when the phases are properly matched.

To demonstrate the applicability of the harmonic averaging method we used, next we calculate the TDSE in the length gauge and model a 1D inhomogeneous field. The wavelength and FWHM of the driving field are the same as those in Fig. 4. Details can be found in Sec. II B. When the FWHM of the inhomogeneous field in real space is 100 nm, the spectrum is shown in Fig. 4 with a yellow dashed line, which is in good agreement with the averaged harmonics with 1D weight. We reduce the FWHM of the driving field to 20 nm, the spectrum changes as shown in Fig. 4 with a black dotted line. Driven by this field, the maximum displacement of the electron and hole motion is about 5 nm, the field changes obviously in this range. If the driving field is further tightly focused, considering the tunneling electrons are localized and lack the inherent periodicity, their dynamics will change inevitably. The calculations of the 1D TDSE explain that the weighted average method is applicable to simulate the solid HHG induced by a nonuniform laser when the field varies little over a few nanometers.

This method of averaging harmonics provides an efficient calculation scheme, whereas the calculations under the length gauge can show the interference mechanism in real space intuitively. We add a Gaussian filtering in real space to extract the spatial information of harmonics, and obtain the harmonic spatial profile $\hat{a}(x_0, t)$. For uniform irradiations, since no lattice has particularity in crystals, harmonics at each lattice are the same, so $\hat{a}(x_0, t)$ is a horizontal line (not shown here). The harmonic spatial profile at $t = 0.6T_0$ induced by the nonuniform field used in Fig. 4 is shown in Fig. 6(a); the FWHM in

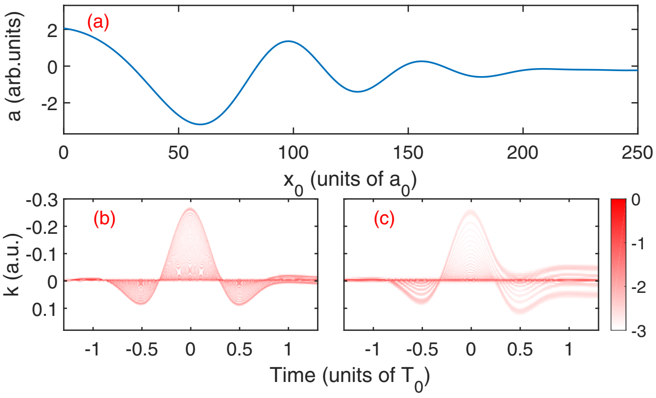

FIG. 6. (a) Harmonic spatial profile $\hat{a}(x_0, t)$ induced by an inhomogeneous field with a FWHM of 200 nm, $t = 0.6T_0$. (b), (c) Evolution of the valence-band electron population driven by the inhomogeneous fields with a FWHM of 100 and 20 nm, respectively. The color scale is logarithmic.

real space is 200 nm. We notice that the spatially dependent harmonic $\hat{a}(x_0, t)$ actually is in agreement with the driving-field-intensity-dependent harmonic $\tilde{a}(F, t)$, when x_0 and F are related by Eq. (4). That is to say, similar to the situation in gases, harmonics generated locally are equivalent to harmonics induced by uniform fields. The inherent phase difference of harmonics caused by the difference of driving field strength is shown as the oscillation of the harmonic spatial profile. This means that, although electrons are nonlocal in crystals, which plays an important role in HHG, different parts of an electron wave can evolve independently without affecting each other on the ultrafast scale. The inherent phase differences shown in Fig. 6(a) plus the phases introduced by the propagation effect determine the harmonic intensity when all harmonics are superimposed. So the harmonic characteristics caused by the nonuniform irradiation essentially come from the interference of harmonics from different lattices in real space.

During the evolution, we project the wave function onto the Bloch states and obtain the population of electrons on each eigenstate. Figures 6(b) and 6(c) show the valence-band populations of an electron with the initial momentum $k = 0$ driven by the inhomogeneous fields with a FWHM of 100 and 20 nm, respectively. The population follows the vector potential of the driving field when the field is homogeneous (not shown here). However, driven by the inhomogeneous field with a FWHM of 100 nm, the electron population is scattered, like the superposition of electrons driven by the fields with different intensities. At the end of the pulse, most electrons return to the initial momentum. But when the FWHM is reduced to 20 nm, most electrons cannot return to the initial point. This further shows that, driven by inhomogeneous fields, electrons are a superposition of many electron states which evolve independently in local areas. And when the driving field changes rapidly on the nanoscale, these local states cannot be considered to be driven by a uniform field.

The discussions in real and momentum spaces show that, when the spatial variation of the laser is slow, similar to the localized electrons in gases, different parts of a Bloch electron can evolve independently without affecting each other on the femtosecond scale. This is why the weighted average method only needs $W(F)$, without considering the specific pattern of the driving laser intensity distribution [note that $F(x)$ uniquely determines $W(F)$, but $W(F)$ cannot uniquely determine $F(x)$]. Therefore, the focus range of the driving lights in the weighted average method is not limited. And in Appendix B, the waist radius of the Gaussian beam is about 80 μm, which is common in experiments. Obviously, this situation makes it easier to meet the application requirements of the weighted-average method because the driving field changes more slowly in space. There are many technologies, such as changing the focus of the laser field, optimizing the size or structure of the target material [20,38], to realize accurate control of the field strength distribution and phase matching on a mesoscopic scale. So the optimization scheme based on inhomogeneous illumination has more operability.

IV. CONCLUSION

In conclusion, when considering inhomogeneous irradiation, the harmonics induced by lasers with different intensities are similar to the longitudinal modes in lasers, and they are in phase when the OPD is appropriate. The optimized OPD can adjust the IPP on the attosecond scale, thus extracting the attosecond time-resolved electron dynamics. The selective enhancement and compression of harmonics in the frequency and time domains can realize a high conversion efficiency of the crystal HHG in some specified energy ranges. Moreover, we find that these interesting phenomena come from the interference of harmonics in real space. The resolution of this interference can reach the nanometer level, which is helpful to study the ultrafast dynamics with nanometer spatial resolution. Our work enriches people's understanding of the phase matching of higher harmonics and provides a key link between experimental and numerical HHG. It will promote the dynamics research with ultrahigh spatial-temporal resolution.

ACKNOWLEDGMENTS

We thank Prof. F. He for stimulating discussions. This work was supported by the National Natural Science Foundation of China (NSFC) (Grants No. 91850121 and No. 11674363), the National Key Research and Development Program of China (Grant No. 2019YFA0307702), and the K. C. Wong Education Foundation.

APPENDIX A: WEIGHTS

In the main text, the weighted average harmonics are in good agreement with the nonuniform-field-induced harmonics calculated under the length gauge. Here, we list the weights in the several specific cases shown in Fig. 1(a). First, a laser with the Gaussian intensity distribution in the cross section irradiates a one-dimensional atomic chain. The driving field that irradiate the atomic chain can be expressed as Eq. (3). Since the crystal density is uniform, the weight in the average can be expressed as dx/dF, i.e., the differential of the function $x = [-\frac{\sigma^2}{4\ln 2}\ln(F/F_0)]^{1/2}$ [the inverse function of Eq. (4)],

$$W(F) \propto \frac{dx}{dF} \propto \frac{1}{[-\ln(F/F_0)]^{1/2}F}. \tag{A1}$$

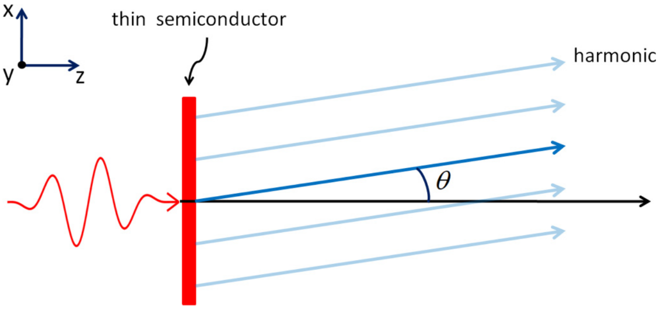

FIG. 7. Schematic diagram of HHG diffraction. The thin semiconductor is perpendicular to the propagation direction of the driving field. The red arrow indicates the driving field and the blue arrows indicate the optical path of harmonics.

This function is called the 1D weight in this paper. Then we consider the atomic distribution in a two-dimensional layer material irradiated by the field. In this case, the differential element in real space corresponding to dF is a ring. So the weight in this case has a simple form, which is a 1D weight multiplied by the inverse function of Eq. (4), i.e.,

$$W(F) \propto \frac{1}{F}, \tag{A2}$$

which is called 2D weight. When considering the longitudinal attenuation of the driving field in a bulk material, the weight can be further changed. We assume that the driving-field intensity decays exponentially along the direction of propagation, and the maximum field strength attenuates to $0.9F_0$. The material is conceived as many layers in our calculations, and the distribution in each layer is a 2D weight. The distribution of all layers added together is called the 3D weight. Note that the average harmonic with 3D weight contains part of the propagation effects [23], that is, the attenuation of the driving pulse during propagation.

APPENDIX B: EXAMPLE OF INTRODUCING OPD AND HARMONIC DIFFRACTION

We assume that a thin semiconductor with negligible thickness is placed vertically in the driving field, as shown in Fig. 7. The focused driving field can be described by a Gaussian beam. The field strength on the material is a two-dimensional Gaussian distribution, and the phase difference of the driving field in the plane of the material is $\Delta\varphi = -k\frac{x^2+y^2}{2z[1+(b/z)^2]}$, where $b = \frac{\pi w_0^2}{\lambda}$ is the confocal parameter and w_0 is the waist radius. Positions with $z < 0$ are usually described as before the focal point, and positions with $z > 0$ are usually described as behind the focal point. Therefore, the OPD of harmonics caused by the propagation in vacuum is

$$D_p = \frac{\Delta\varphi}{k} = -\frac{x^2 + y^2}{2z[1 + (b/z)^2]}. \tag{B1}$$

The diffraction of the near-field harmonics results in the distributions of far-field harmonics. The OPD corresponding to the diffraction angle θ shown in Fig. 7 is

$$D_d \approx x\theta. \tag{B2}$$

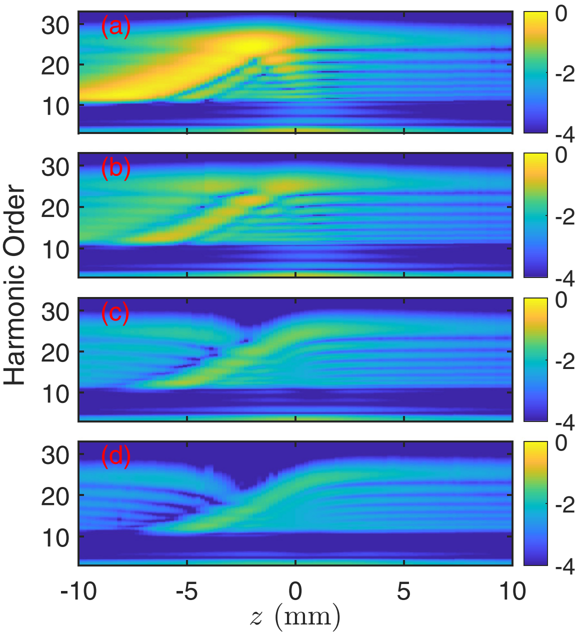

FIG. 8. Location- and diffraction-angle-dependent HHG spectra. (a)–(d) correspond to $\theta = 0$, 0.001, 0.002, and 0.003 rad, respectively. The color scale is logarithmic.

It leads to the transverse spatial distribution of far-field harmonics.

In the simulation, we uniformly pick points in the plane of the material and coherently superimpose all the harmonics in these points after adding the OPD of $D_p + D_d$. The z- and θ-dependent harmonic spectra are obtained during the calculations with different angles and positions, which are shown in Fig. 8. $b = 6$ mm, and other parameters of the driving field are similar to those in Fig. 4 in the main text. To avoid the variations of harmonic spectrum caused by the change of peak field strength when changing the position of the material, the peak intensity of the driving field is fixed. In experiments, the intensity attenuation caused by the material away from the focus can be compensated by increasing the intensity of the laser. We can see that the spectra vary with angle, but the harmonics are mainly distributed near the z axis ($\theta = 0$). Therefore, when considering the variation of harmonic intensities, it is reasonable to consider only the harmonic on the z axis.

It can be seen in Fig. 8(a) that the harmonic yield is high when the material is placed in front of the focus, while the yield decreases significantly when the material moves behind the focus. This is qualitatively similar to the gas HHG experiments [14]. In addition, a remarkable feature is that, before the focus, the enhanced harmonic energy increases gradually as the material approaches the focus. That is, harmonics are selectively enhanced by the position of the material. For example, the positions where the 15th and 25th harmonics are enhanced are -6 and -2 mm, respectively, the D_p at these positions are shown in Fig. 9. It can be seen that these D_p are very close to the optimal OPD for enhancing the 15th and 25th harmonics in the main text. The D_p after the focus is negative, which corresponds to the OPD

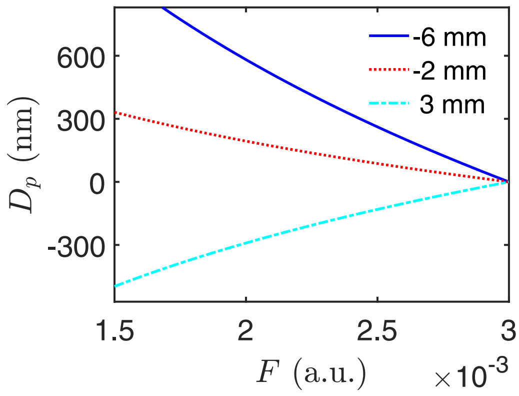

FIG. 9. The driving-field-strength-dependent D_p on the Gaussian beam cross section.

for suppressing harmonics. Therefore, we show an example of selectively enhancing harmonics by introducing OPD through the propagation of a driving field in the vacuum. As revealed in the main text, the introduction of OPD accurately moves the IPP in the time domain. The harmonics at the IPP are enhanced, and the harmonics far away from the IPP are suppressed. Therefore, the z-dependent enhanced harmonics come from harmonics selected in the time domain; indeed, Fig. 8(a) is the mirror image of Fig. 5(a) in the main text. So we demonstrate the feasibility of observing and controlling HHG within attosecond resolution. Specifically, the weakening of long trajectories caused by the localization or dephasing of electrons can be manifested in Fig. 8(a) as the rapid attenuation of harmonic yields at positions away from $z = 0$.

[1] A. E. Siegmann, *Lasers* (University Science Books, Mill Valley, 1986).
[2] A. McPherson, G. Gibson, H. Jara, U. Johann, T. S. Luk, I. A. McIntyre, K. Boyer, and C. K. Rhodes, J. Opt. Soc. Am. B **4**, 595 (1987).
[3] P. B. Corkum, Phys. Rev. Lett. **71**, 1994 (1993).
[4] M. Lewenstein, P. Balcou, M. Y. Ivanov, A. L'Huillier, and P. B. Corkum, Phys. Rev. A **49**, 2117 (1994).
[5] F. H. M. Faisal and J. Z. Kamiński, Phys. Rev. A **56**, 748 (1997).
[6] K. A. Pronin and A. D. Bandrauk, Phys. Rev. Lett. **97**, 020602 (2006).
[7] S. Ghimire, A. D. DiChiara, E. Sistrunk, P. Agostini, L. F. DiMauro, and D. A. Reis, Nat. Phys. **7**, 138 (2011).
[8] G. Vampa, C. R. McDonald, G. Orlando, D. D. Klug, P. B. Corkum, and T. Brabec, Phys. Rev. Lett. **113**, 073901 (2014).
[9] K. K. Hansen, T. Deffge, and D. Bauer, Phys. Rev. A **96**, 053418 (2017).
[10] T. T. Luu, Z. Yin, A. Jain, T. Gaumnitz, Y. Pertot, J. Ma, and H. J. Wörner, Nat. Commun. **9**, 3723 (2018).
[11] T. T. Luu and H. J. Wörner, Phys. Rev. A **98**, 041802(R) (2018).
[12] C. Yu, K. K. Hansen, and L. B. Madsen, Phys. Rev. A **99**, 063408 (2019).
[13] A. W. Zeng and X. B. Bian, Phys. Rev. Lett. **124**, 203901 (2020).
[14] P. Salières, A. L'Huillier, and M. Lewenstein, Phys. Rev. Lett. **74**, 3776 (1995).
[15] P. Antoine, A. L'Huillier, and M. Lewenstein, Phys. Rev. Lett. **77**, 1234 (1996).
[16] E. Constant, D. Garzella, P. Breger, E. Mével, C. Dorrer, C. Le Blanc, F. Salin, and P. Agostini, Phys. Rev. Lett. **82**, 1668 (1999).
[17] C. G. Durfee, III, A. R. Rundquist, S. Backus, C. Herne, M. M. Murnane, and H. C. Kapteyn, Phys. Rev. Lett. **83**, 2187 (1999).
[18] T. Popmintchev *et al.*, Science **336**, 1287 (2012).
[19] M. Sivis, M. Duwe, B. Abel, and C. Ropers, Nat. Phys. **9**, 304 (2013).
[20] G. Vampa *et al.*, Nat. Phys. **13**, 659 (2017).
[21] M. Blanco, C. Hernández-García, A. Chacón, M. Lewenstein, M. T. Flores-Arias, and L. Plaja, Opt. Express **25**, 14974 (2017).
[22] C. Q. Abadie, M. Wu, and M. B. Gaarde, Opt. Lett. **43**, 5339 (2018).
[23] I. Floss, C. Lemell, G. Wachter, V. Smejkal, S. A. Sato, X.-M. Tong, K. Yabana, and J. Burgdörfer, Phys. Rev. A **97**, 011401(R) (2018).
[24] G. Vampa, T. J. Hammond, N. Thiré, B. E. Schmidt, F. Légaré, C. R. McDonald, T. Brabec, and P. B. Corkum, Nature (London) **522**, 462 (2015).
[25] G. Vampa, C. R. McDonald, G. Orlando, P. B. Corkum, and T. Brabec, Phys. Rev. B **91**, 064302 (2015).
[26] S. Ghimire *et al.*, J. Phys. B: At., Mol. Opt. Phys. **47**, 204030 (2014).
[27] N. Yoshikawa, T. Tamaya, and K. Tanaka, Science **356**, 736 (2017).
[28] G. Ndabashimiye, S. Ghimire, M. Wu, D. A. Browne, K. J. Schafer, M. B. Gaarde, and D. A. Reis, Nature (London) **534**, 520 (2016).
[29] T.-Y. Du, Z. Guan, X.-X. Zhou, and X.-B. Bian, Phys. Rev. A **94**, 023419 (2016).
[30] M. F. Ciappina *et al.*, Rep. Prog. Phys. **80**, 054401 (2017).
[31] I. Kilen, M. Kolesik, J. Hader, J. V. Moloney, U. Huttner, M. K. Hagen, and S. W. Koch, Phys. Rev. Lett. **125**, 083901 (2020).
[32] M. Korbman, S. Yu Kruchinin, and V. S. Yakovlev, New J. Phys. **15**, 013006 (2013).
[33] C. Chandre, S. Wiggins, and T. Uzer, Physica (Amsterdam) **181D**, 171 (2003).
[34] L. V. Keldysh, J. Exp. Theor. Phys. **47**, 1945 (1964) [Sov. Phys. JETP **20**, 1307 (1965)].
[35] J. Tate, T. Auguste, H. G. Muller, P. Salières, P. Agostini, and L. F. DiMauro, Phys. Rev. Lett. **98**, 013901 (2007).
[36] T.-Y. Du, D. Tang, X.-H. Huang, and X.-B. Bian, Phys. Rev. A **97**, 043413 (2018).
[37] J. B. Li, S. L. Fu, H. Q. Wang, X. Zhang, B. W. Ding, B. T. Hu, and H. C. Du, Phys. Rev. A **98**, 043409 (2018).
[38] S. Han, H. Kim, Y. W. Kim, Y. J. Kim, S. Kim, I. Y. Park, and S. W. Kim, Nat. Commun. **7**, 13105 (2016).